# Crystallographic facet heterojunction of MIL-125-NH$_2$(Ti) for carbon dioxide photoreduction

Xiao-Mei Cheng [a,b], Yuming Gu [c], Xiao-Yu Zhang [a], Xiao-Yao Dao [a], Shi-Qing Wang [a], Jing Ma [c,*], Jing Zhao [b,*], Wei-Yin Sun [a,*]

[a] Coordination Chemistry Institute, State Key Laboratory of Coordination Chemistry, School of Chemistry and Chemical Engineering, Nanjing National Laboratory of Microstructures, Collaborative Innovation Center of Advanced Microstructures, Nanjing University, Nanjing, 210023, China
[b] State Key Laboratory of Coordination Chemistry, Chemistry and Biomedicine Innovation Center (ChemBIC), School of Chemistry and Chemical Engineering, Nanjing University, Nanjing, 210023, China
[c] Key Laboratory of Mesoscopic Chemistry of Ministry of Education, School of Chemistry and Chemical Engineering, Nanjing University, Nanjing, 210023, China

## ARTICLE INFO

## ABSTRACT

Facet exposure affects photocatalytic CO$_2$ reduction reaction, but the insight remains unclear. Here, we report finely controlled six types of MIL-125-NH$_2$(Ti) exposing single and co-exposing mixed low-index facets as model catalysts and provide an insight into facet effect on photoreduction of CO$_2$. Facet surface heterojunction endows MIL-125-NH$_2$(Ti) with a broadened light-absorption and accelerated charge migration. The MIL-125-NH$_2$(Ti) with {110}/{111}-heterojunction yields ca. 10 and 18 times enhanced CO$_2$ reduction to CO and CH$_4$ compared with the single {001} facet exposed. Density functional theory (DFT) calculations provide an energetically favorable CO$_2$ catalytic reduction pathway and identify the rate-limiting step on different low-index facets. This work aims at exploring facet-effect on CO$_2$ photoreduction, understanding the facet-dependence and providing a paradigm for MOFs materials by regulating facet to enhance the general surface catalytic reaction activity.

## 1. Introduction

Facets with distinctive crystallographic characteristics possess different surface configurations, resulting in a great difference in photocatalytic performance [1–3]. Facet tailoring directly affects the surface electronic structures, optical properties and electron transport characteristics of the catalysts [4–6]. The facet-dependent catalytic activity has been observed in varied catalytic reactions, and the activities are often sensitive to the well-defined facets [7–9]. For inorganic semiconductor materials, TiO$_2$ is one of the most investigated materials in facet engineering [10–13], especially for {101} and {001} facets due to their excellent redox performance [14,15]. In 2014, Yu et al. reported a breakthrough in photocatalytic CO$_2$ reduction over TiO$_2$ with co-exposed {001}/{101} facets and proposed a new concept of "surface heterojunction" by DFT calculations [16]. However, studies regarding the facet effect, much less the surface heterojunction, of metal-organic frameworks (MOFs) in the photocatalytic process were barely reported [17,18].

MOFs are composed of metal ions or clusters connected by organic ligands [19,20]. The tunability of metal centers and modifiability of

ligands are advantageous regarding the capability of precisely designing and tailoring structure at the atomic level for MOFs materials [21–25]. The features of high specific surface area, CO$_2$ adsorption capacity and tunable porosity endow MOFs as a desired platform for photocatalysis [26,27]. Photocatalytic reaction, as a typical surface reaction, is sensitively influenced by active sites on the surface of photocatalyst as well as CO$_2$ adsorption capacity and electron migration ability [28–30]. Thus, the regulation of facets in MOFs is vital to the photoreduction reaction of CO$_2$.

Herein, we report a series of MIL-125-NH$_2$(Ti) with finely controlled single low-index facets including {001}, {110} and {111}, and mixture of co-exposed low-index facets of {001}/{110}, {001}/{111} and {110}/{111} to investigate facet-effect on photocatalytic CO$_2$ reduction. All MIL-125-NH$_2$(Ti) MOFs have photoreduction ability for converting CO$_2$ into CO and CH$_4$. The possibility of MIL-125-NH$_2$(Ti) for the photocatalytic system was further verified by calculations of the partial density of states (PDOS). The facet-effect on photoreduction of CO$_2$ reduction was revealed through the catalyst structure characterization and performance experiments. The results suggest that co-exposed {110}/{111} facets of MIL-125-NH$_2$(Ti) possess superior

photocatalytic activity since the {110}/{111} facets co-exposed form a surface heterojunction, which is favorable for accelerating electron transfer, inhibiting photogenerated carriers recombination, thereby improving photocatalytic efficiency. Furthermore, density functional theory (DFT) calculations revealed the energetically favorable reaction pathway for photocatalytic $CO_2$ reduction over MIL-125-$NH_2$(Ti) with low-index {001}, {110} and {111} facets.

## 2. Experimental section

### 2.1. Synthesis of MIL-125-NH₂(Ti) with different facets

{001} facets (T1): DMF (7.0 mL) was mixed with MeOH (3.0 mL) to form the mixed solvent. 0.34 g of $NH_2$-BDC and 1.12 g of CTAB were dispersed into an above mentioned mixed solvent with sonication. Then, 0.25 mL of TBOT was added and continuous ultrasonication for 5 min. The yellow solution was sealed into the Teflon-line steel autoclave, and kept in an oven at 150 °C for 8 h. The yellow powders were separated by centrifuging, washed with DMF three times, and ethanol five times, and fully dried in vacuum oven for 5 h at 80 °C.

{110} facets (T2): 9.0 mL of DMF and 1.0 mL of MeOH form the mixed solvent. 0.28 g of $NH_2$-BDC was dispersed into the above mentioned mixed solvent with sonication. Then, 0.34 mL of TBOT and 0.27 mL of AA were added and continuous ultrasonication for 5 min. The yellow solution was sealed into the Teflon-line steel autoclave, and kept in an oven at 150 °C for 24 h. The yellow powders were separated by centrifuging, washed with DMF three times, and ethanol five times, and fully dried in vacuum oven for 5 h at 80 °C.

{111} facets (T3): 9.0 mL of DMF and 1.0 mL of MeOH to form the mixed solvent. 0.14 g of $NH_2$-BDC was dispersed into the above mentioned mixed solvent with sonication. Then, 0.15 mL of TPOT and 0.53 mL of AA were added and continuous ultrasonication for 5 min. The yellow solution was sealed into the Teflon-line steel autoclave, and kept in an oven at 150 °C for 24 h. The yellow powders were separated by centrifuging, washed with DMF three times, and ethanol five times, and fully dried in vacuum oven for 5 h at 80 °C.

{001}/{110} facets (T12): 7.0 mL of DMF and 3.0 mL of MeOH to form the mixed solvent. 0.21 g of $NH_2$-BDC and 0.25 mL of TBOT were dispersed into the above mentioned mixed solvent with sonication. The yellow solution was sealed into the Teflon-line steel autoclave, and kept in an oven at 150 °C for 8 h. The yellow powders were separated by centrifuging, washed with DMF three times, and ethanol five times, and fully dried in vacuum oven for 5 h at 80 °C.

{001}/{111} facets (T13): 2.7 mL of DMF and 0.3 mL of MeOH to form the mixed solvent. 0.11 g of $NH_2$-BDC and 0.17 mL of TBOT were added into the above mentioned mixed solvent with sonication. The yellow solution was sealed into the Teflon-line steel autoclave, and kept in an oven at 150 °C for 24 h. The yellow powders were separated by centrifuging, washed with DMF three times, and ethanol five times, and fully dried in vacuum oven for 5 h at 80 °C.

{110}/{111} facets (T23): 9.0 mL of DMF and 1.0 mL of MeOH form the mixed solvent. 0.14 g of $NH_2$-BDC was dispersed into the above mentioned mixed solvent with sonication. Then, 0.15 mL of TPOT and 0.80 mL of AA were added and continuous ultrasonication for 5 min. The yellow solution was sealed into the Teflon-line steel autoclave, and kept in an oven at 150 °C for 24 h. The yellow powders were separated by centrifuging, washed with DMF three times, and ethanol five times, and fully dried in vacuum oven for 5 h at 80 °C.
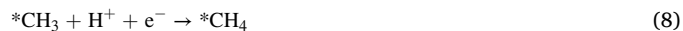
### 2.2. Density functional theory (DFT) calculations

All of the density functional theory (DFT) calculations were carried out using the Vienna ab initio simulation package (VASP) based on the projector augmented wave (PAW) method [31,32]. The generalized gradient approximation (GGA) method together with the Perdew-Burke-Ernzerhof (PBE) as exchange-correlation functional was employed in both geometry optimizations and electronic property calculations [33]. The Grimme method was applied to take the van der Waals interaction into consideration, and the cutoff kinetic energy was set to be 450 eV [34,35]. The Hubbard-like + U approach [36] was used to treat the Ti atoms with the effective $U_{eff}$, $U_{eff} = U − J = 7.0$ eV for Ti atoms [37]. Three slab models in periodic boundary condition (PBC) were built to study the $CO_2$ conversion pathways on (001), (110) and (111) surfaces, respectively (Table S7). The vacuum thickness was set to be 15 Å to avoid the interactions between the adjacent cells. It is recognized that in many cases PBE functional would underestimate the bandgap of the materials, which has been demonstrated in recent works [38–41]. The employment of HSE06 functional may relieve this problem. However, the number of the simulated model for (111) surface is about 300 atoms in a cuboid box with periodical boundary condition (PBC). The $CO_2$-to-$CH_4$ reduction reaction is a complex process with the involvement of eight protons and electrons. For studying of the $CO_2$-to-$CH_4$ process systematically, it may be difficult to examine the different reaction pathways on three different surface facets, i.e. (001), (110), (111), with the expensive HSE06 functional for about 30 intermediates. The energy convergence value between two consecutive steps was chosen as $1 \times 10^{-4}$ eV, and a maximum force was allowed lower than 0.04 eV/Å on each atom.

The $CO_2$ reduction reaction process can be described by eight basic steps:

$$* + CO_2 + H^+ + e^- \rightarrow *COOH \tag{1}$$

$$*COOH + H^+ + e^- \rightarrow *CO + H_2O \tag{2}$$

$$*CO + H^+ + e^- \rightarrow *CHO \tag{3}$$

$$*CHO + H^+ + e^- \rightarrow *CH_2O \tag{4}$$

$$*CH_2O + H^+ + e^- \rightarrow *CH_3O \tag{5}$$

$$*CH_3O + H^+ + e^- \rightarrow *CH_3OH \tag{6}$$

$$*CH_3OH + H^+ + e^- \rightarrow *CH_3 + H_2O \tag{7}$$

$$*CH_3 + H^+ + e^- \rightarrow *CH_4 \tag{8}$$

in which * represents the MIL-125-$NH_2$(Ti) surface. The Gibbs free energy changes can be calculated by the following Eqs.

$$\Delta G_{*COOH} = G(*COOH) - G(*) - G(CO_2) + 1/2\, G(H_2) \tag{9}$$

$$\Delta G_{*CO} = G(*CO) - G(*) - G(CO_2) + G(H_2O) + G(H_2) \tag{10}$$

$$\Delta G_{*CHO} = G(*CHO) - G(*) - G(CO_2) + G(H_2O) + 3/2\, G(H_2) \tag{11}$$

$$\Delta G_{CH2O} = G(*CH_2O) - G(*) - G(CO_2) + G(H_2O) + 2\, G(H_2) \tag{12}$$

$$\Delta G_{*CH3O} = G(*CH_3O) - G(*) - G(CO_2) + G(H_2O) + 5/2\, G(H_2) \tag{13}$$

$$\Delta G_{*CH3OH} = G(*CH_3OH) - G(*) - G(CO_2) + G(H_2O) + 3\, G(H_2) \tag{14}$$

$$\Delta G_{*CH3} = G(*CH_3) - G(*) - G(CO_2) + 2\, G(H_2O) + 7/2\, G(H_2) \tag{15}$$

$$\Delta G_{*CH4} = G(*CH_4) - G(*) - G(CO_2) + 2\, G(H_2O) + 4\, G(H_2) \tag{16}$$

where G(*), G(*COOH), G(*CO), G(*CHO), G(*CH₂O), G(*CH₃O), G (*CH₃OH), G(*CH₃), and G(*CH₄) are the free energies of MIL-125-$NH_2$(Ti) surface, and that adsorbed by *COOH, *CO, *CHO, *CH₂O, *CH₃O, *CH₃OH, *CH₃, and *CH₄ intermediates, respectively. G($CO_2$), G($H_2O$), and G($H_2$) are the free energies of gaseous $CO_2$, $H_2O$, and $H_2$ molecules, respectively. The G values for each gaseous and adsorbed species are calculated by:
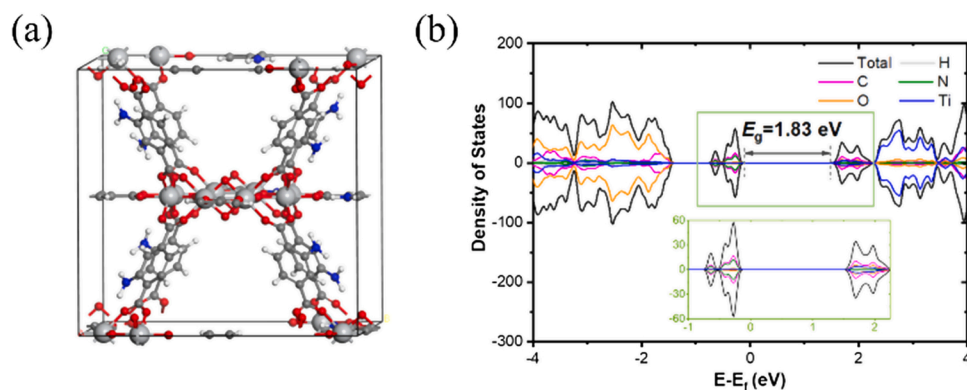
**Fig. 1.** The crystal structure (a) and partial density of states (PDOS) of MIL-125-NH$_2$(Ti) at PBE + U level (b).

$$G = E_{total} + E_{ZPE} - TS \qquad (17)$$

E$_{total}$ is the total energy from the DFT calculations. E$_{ZPE}$ is the zero-point energy, S is the entropy, and T is the temperature.

### 2.3. Photocatalytic CO$_2$ reduction

The photoreduction of CO$_2$ experiment was carried out in CEL-SPH2N-D9 (CeAulight, China) with a condensate circulating water filter to avoid the photothermal effect. Firstly, 5 mg of the as-synthesized
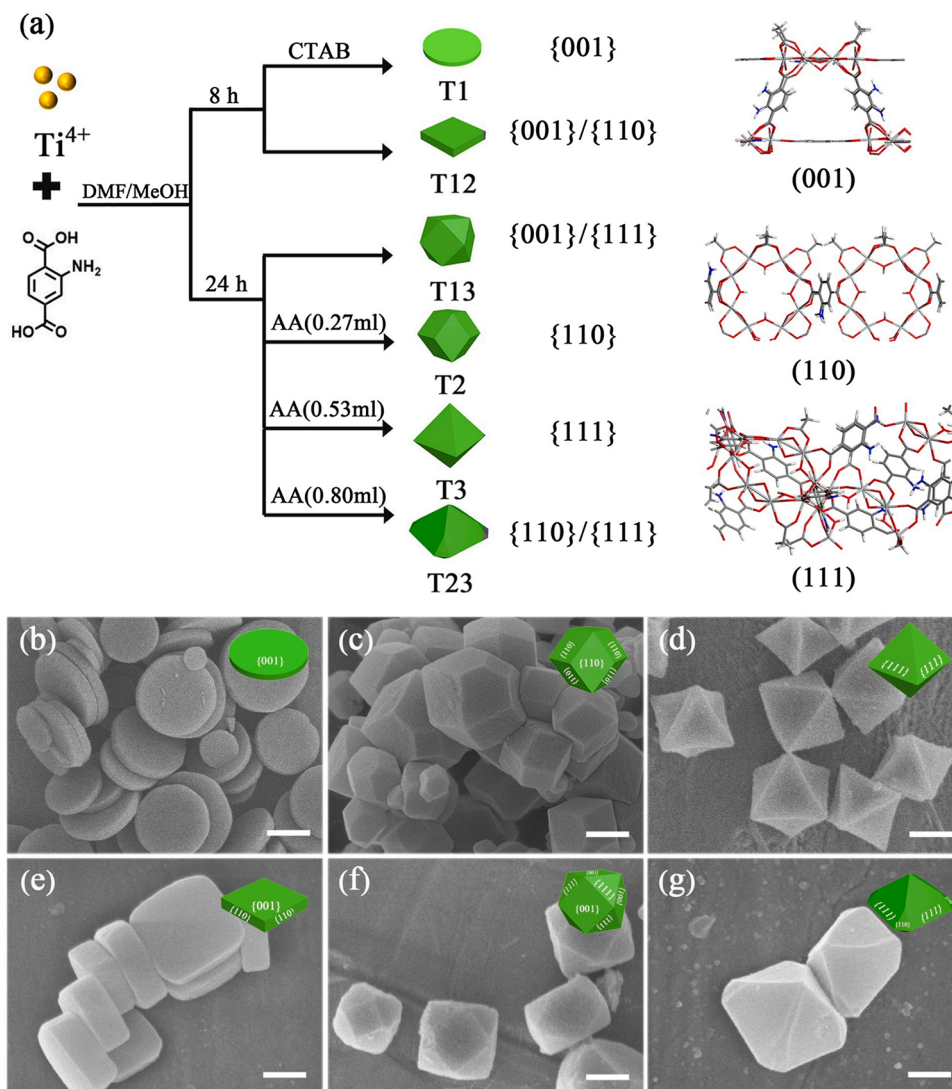


**Fig. 2.** (a) Schematic illustration of the evolution of morphology and facet over MIL-125-NH$_2$(Ti). SEM images of as-synthesized MIL-125-NH$_2$(Ti) with disk-shaped plate (T1) (b), rhombic dodecahedron (T2) (c), octahedron (T3) (d), rectangle-like plate (T12) (e), truncated cube (T13) (f) and truncated octahedron (T23) (g). Scale bar: 500 nm.

photocatalysts were scattered in 15 mL MeCN and 1 mL water with 3 mL TEOA as a sacrificial agent, ultra-sonicated to form a suspension, and pour into the reaction cell (d =4 cm). In a vacuum reaction system, pure $CO_2$ gas (80 kPa, 99.999 %, Shangyuan Gas) was injected with a 4 °C condenser circulation pump. A 300 W xenon arc lamp with AM 1.5 G filter (100 mW/cm$^2$) was used as the light source and vertically placed outside the reactor. Every 1 h, 1.0 mL of reactive gas were taken from the reactor with the online automatic gas sampling system (CEL-GSOA-1). The gas products were detected by gas chromatography (GC-9860) with a flame ionized detector (FID). The retention time of CO and $CH_4$ are 1.290 and 2.370 min. All photocatalytic data were repeated at least three times. Recycling experiments were performed under similar conditions by using a collected catalyst instead of a fresh catalyst.

### 2.4. Electrochemical measurements

The electrochemical measurements including electrochemical impedance spectroscopy (EIS) and Mott-Schottky test were performed on the Zahner electrochemical workstation with standard three-electrode system. Carbon cloth and photocatalyst-coated glassy carbon as the working electrode for EIS and Mott-Schottky test, graphite rod as the counter electrode and Ag/AgCl electrode as the reference electrode. 0.2 M of $Na_2SO_4$ solution and the mixed solution of 0.5 M of KCl solution and 0.01 M of $K_3[Fe(CN)_6]/K_4[Fe(CN)_6]$ with a ratio of 1:1 were used as the electrolyte for Mott-Schottky and EIS test, respectively.

The cyclic voltammetry curve was measured on a CHI 730E electrochemical workstation with a standard three-electrode system with a scan rate of 0.1 V/s. Platinum wire and Ag/AgCl electrode as the counter and refence electrode. The working electrode was ITO coated with samples. The curves were obtained for the electrolyte in MeCN with tetrabutylammonium hexafluorophosphate (0.1 M). The inks were prepared by utrasonication of 2 mg samples in a 1.05 mL mixed solution (Nafion: $H_2O$: isopropanol = 1:10:10) for 30 min and dropping 100 μL of the suspension onto the ITO electrode.

### 2.5. Photoelectrochemical measurements

Transient photocurrent measurements were measured on a CHI 730E electrochemical workstation in a standard three-electrode system. Graphite rod, ITO plate(1 cm$^2$) and Ag/AgCl electrode as counter, working and reference electrode, respectively. $Na_2SO_4$ (0.2 M) solution as the electrolyte. Switch light at least 10 recycles.

### 2.6. Quantum yield

The quantum yield of $CO_2$ photocatalytic conversion in 5 h can be calculated by following Eqs. (18) and (19). Two and eight electrons are required to convert $CO_2$ to CO and $CH_4$, respectively [42,43].

$$\phi_{CO} (\%) = \frac{2 \times \text{mole of CO formation}}{\text{mole of photons absorbed by photocatalyst}} \qquad (18)$$

$$\phi_{CH_4} (\%) = \frac{8 \times \text{mole of } CH_4 \text{ formation}}{\text{mole of photons absorbed by photocatalyst}} \qquad (19)$$

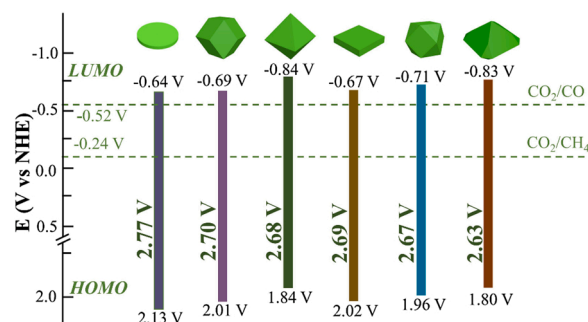The number of moles of photons absorbed by photocatalyst (MPAP) during 5 h was calculated by Eq. (20).



**Fig. 3.** HOMO-LUMO gap of the as-synthesized MIL-125-$NH_2$(Ti).

## 3. Results and discussion

### 3.1. Partial density of states (PDOS) of MIL-125-$NH_2$(Ti)
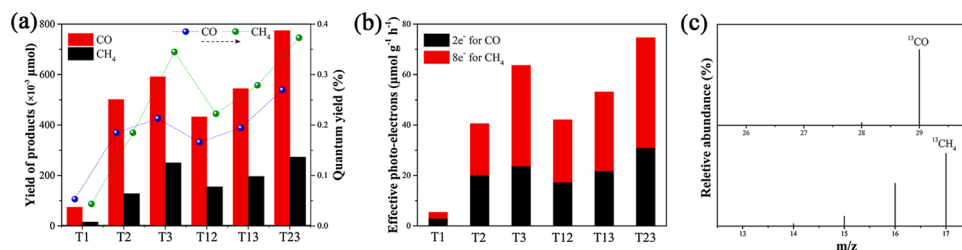
To explore the possibility of photocatalytic performance of MIL-125-$NH_2$(Ti) during the $CO_2$ reduction reaction process, the partial density of states (PDOS) was calculated by DFT. The MIL-125-$NH_2$(Ti) displayed semiconductor property with a bandgap ($E_g$) of 1.83 eV as shown in Fig. 1. The low $E_g$ value indicates that MIL-125-$NH_2$(Ti) possesses a good capacity for absorbing light to improve the efficiency of $CO_2$ conversion. The bandgap was 1.51 eV without GGA + U approach (Fig. S1), indicating that taking the on-site coloumbic repulsion into account was important to describe the electronic structure of transition metal atoms [44]. Moreover, the conduction-band minimum (CBM) is mainly composed of Ti 3d orbitals. The valence-band maximum (VBM) is dominated by C 2p and N 2p orbitals, thus the Ti center may play the role of the active site for the $CO_2$ conversion.

### 3.2. Morphologies of catalysts

Based on the above mentioned results, the study of MIL-125-$NH_2$(Ti) with different facets on photocatalytic $CO_2$ reduction is a compelling project. As shown in Fig. 2a, the specific facets and morphologies of MIL-125-$NH_2$(Ti) were achieved by changing the reaction time, DMF-MeOH solvent ratio and modulator in the reaction. Powder X-ray diffraction (PXRD) patterns were used to characterize the crystal phases of these as-synthesized MIL-125-$NH_2$(Ti). All the samples display similar PXRD patterns (Fig. S2), which are in agreement well with the calculated MIL-125-$NH_2$(Ti) [45]. Herein, the {hkl} indicates the set of all planes that are equal to (hkl) by the lattice symmetry, and h, k and l mean Miller index [46]. The identification and calculation of low-index crystallographic facet including {001}, {110} and {111} facets are presented in Fig. S3 [47]. The relationship between the morphology and crystal plane is further supported by Steno's law, namely the angles between two corresponding facets on the crystals are constant, thus the crystallographic facet can be defined [48,49], and the results are shown in Fig. S4 and Table S1.

Scanning electron microscopy (SEM) images reveal the morphology and facet features of these as-synthesized samples directly. The low-index crystallographic facets of {001}, {110} and {111} are exposed as exhibited in Fig. 2b, c and d, displaying different morphologies with disk-shaped plate, rhombic dodecahedron and octahedron, which are named as T1, T2 and T3, respectively. Fig. 2e shows the morphology of MIL-125-$NH_2$(Ti) with rectangle-like plates consisting of {001} and

$$\text{MPAP} = \frac{\text{absorbed photon flux} \left(\frac{\mu W}{cm^2}\right) \times \text{outer surface area of reactor } (cm^2) \times \text{radiation time (s)}}{\text{each photo energy J} \times (6.02 \times 10^{23})} \qquad (20)$$

**Fig. 4.** The yield of products (a) and effective photo-electrons (b) of CO and $CH_4$ after irradiation for 5 h over the as-synthesized MIL-125-$NH_2$(Ti), (c) $^{13}C$-isotope trace test by using T23 as photocatalyst.

{110} facets, donated as T12. {001} and {111} mixed facets construct a truncated cube (Fig. 2f), and {111} and {110} facets build a truncated octahedron (Fig. 2g) of samples, which are set to T13 and T23, respectively. Fourier transform infrared (FTIR) spectroscopy (Fig. S5) and X-ray photoelectron spectroscopy (XPS) (Figs. S6-S11) were employed to clarify the functional groups and surface chemical state in these samples. In addition, the Ti element atomic concentrations of these samples were listed in Table S2, which indicates the varied exposure degree of the metal-oxo cluster on different facets.

### 3.3. Optical properties and band structure of catalysts

To explore the optical properties and band structure of the as-synthesized MIL-125-$NH_2$(Ti), UV–vis diffuse reflectance spectra (DRS) were measured. The results show the effectively broadened light absorption range by tuning the facet exposure of the samples (Fig. S12). The corresponding gaps between the highest occupied molecular orbital (HOMO) and the lowest unoccupied molecular orbital (LUMO) for T1, T2, T3, T12, T13 and T23 were calculated to be 2.77, 2.70, 2.68, 2.69, 2.67 and 2.63 eV by Tauc plots derived from the DRS (Fig. S13),

respectively [50–52]. Mott-Schottky plots were further employed to definite the HOMO-LUMO gap edges of the samples since that all samples as typical n-type semiconductors (Fig. S14) [53]. All the results of measurements and calculations are shown in Fig. 3, the LUMO energy level was more negative than the reduction potential of thermodynamic requirements of photocatalytic conversion of $CO_2$-to-CO (-0.52 V vs NHE) and $CO_2$-to-$CH_4$ (-0.24 V vs NHE) [54]. Thus, MIL-125-$NH_2$(Ti) has promising potential for photoreduction of $CO_2$.

### 3.4. Photocatalytic $CO_2$ reduction of catalysts

The photocatalytic $CO_2$ reduction performances of as-synthesized catalysts were evaluated by simulated sunlight-driven photoreduction experiments conducted under a $CO_2$-saturated $CH_3CN/H_2O$ ($v:v = 15:1$) system with triethanolamine (TEOA) as sacrificial electron donor. All samples demonstrated to have the ability for conversion of $CO_2$ to CO and $CH_4$ under simulated sunlight irradiation. The CO and $CH_4$ were detected by gas chromatography with FID detector (Fig. S15). Fig. 4a shows the reduction products yields with different catalysts, and the detailed catalytic performance data are listed in Table S3, T23 with
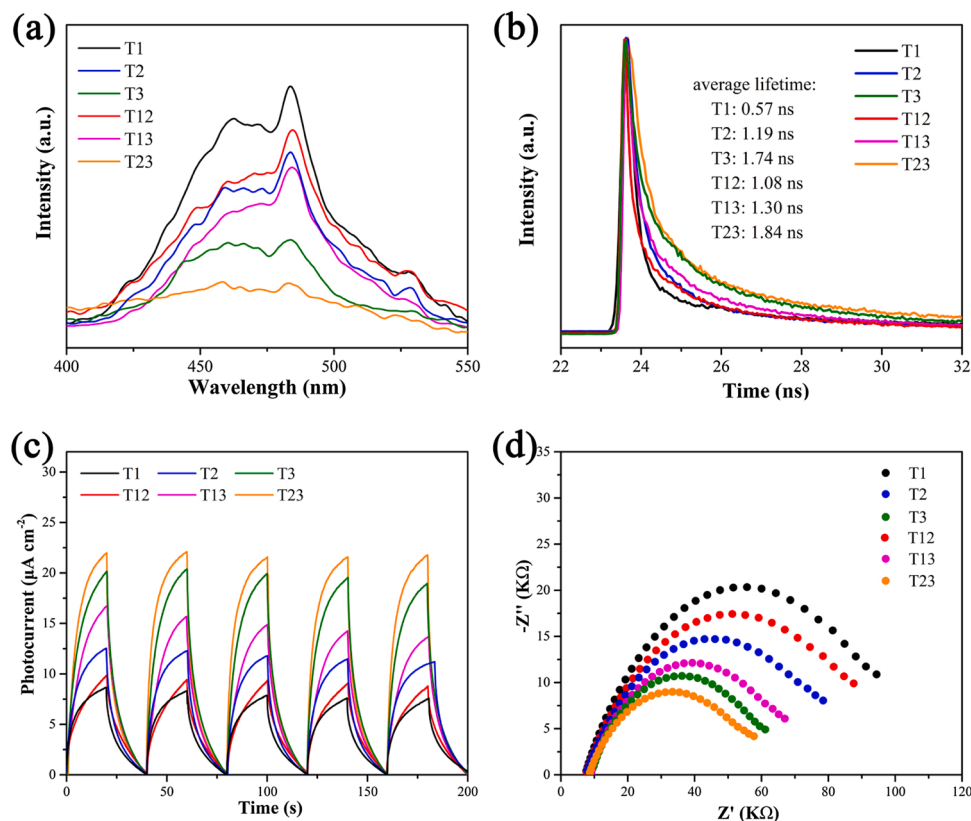


**Fig. 5.** (a) Steady PL spectra under 325 nm excitation, (b) time-resolved fluorescence decay spectra, (c) photocurrent transient response, and (d) EIS Nyquist plots of the as-synthesized photocatalysts.
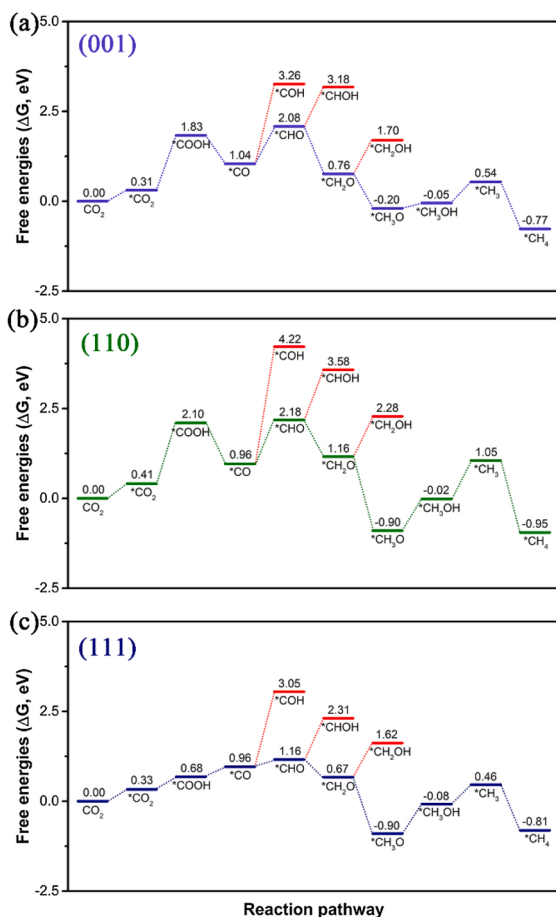
**Fig. 6.** Free energy diagrams of photocatalytic reduction pathways of $CO_2$-to-CO and $CO_2$-to-$CH_4$ for MIL-125-$NH_2$(Ti) on (a) (001), (b) (110) and (c) (111) surfaces.

detected in the photocatalytic system ensured by ^{1}H-NMR spectral measurements (Fig. S16). The TEOA was oxidized during the photocatalytic process (Fig. S17). The ^{13}C-isotope trace test by using [13]$CO_2$ as a reduction substrate in the photoreduction of $CO_2$ confirms that the CO and $CH_4$ originated from the $CO_2$, rather than the decomposition of the organic framework of the catalysts (Fig. 4c) [55]. All the as-synthesized MIL-125-$NH_2$(Ti) samples exhibit good stability after 5 recycles (Fig. S18). The PXRD patterns, SEM images and FTIR spectra of all the catalysts after 5 recycles confirmed the stability of crystal phases, morphology and functional groups (Figs. S19-S21). The above results further demonstrated the excellent stability of as-synthesized MIL-125-$NH_2$(Ti) in $CO_2$ photoreduction reaction.

### 3.5. Photocatalytic mechanism

In addition to the optical properties and band structure, large specific surface area and high $CO_2$ adsorption capacity are the essential requisites for photocatalytic $CO_2$ reduction [28]. Thus, $N_2$ and $CO_2$ adsorption isotherms of the as-synthesized samples were measured (Figs. S22-S24). The results are listed in Table S5, T23 possesses the largest specific surface area and the highest $CO_2$ uptakes, providing more adsorption and activation sites for $CO_2$ substrate. To further understanding the photogeneration charge separation and transfer abilities, photoluminescent (PL) and time-resolved fluorescence decay experiments were carried out. T1 has a high PL emission, which is attributed to the recombination of electron-hole pairs while T23 exhibits a fast electron transfer ability with a prolonged carrier lifetime as well as low PL peak intensity (Fig. 5a and b). The average carrier lifetime decreases in the order of T23 (1.84 ns) > T3 (1.74 ns) > T13 (1.30 ns) > T2 (1.19 ns) > T12 (1.08 ns) > T1 (0.57 ns). In order to show the intrinsic properties and the state of all the samples at different potentials, the cyclic voltammetry curves were tested (Fig. S25) [56]. Moreover, to further evaluate the separation and migration efficiency of charge carriers, the photocurrent transient response (Fig. 5c) was examined. All the catalysts show a significant photocurrent response under irradiation. Obviously, T23 shows the strongest photocurrent density than the others, indicating that charge separation and migration efficiency of T23 was improved by exposing {110} and {111} facets. In Fig. 5d, the smallest semicircle radius for T23 was presented in Nyquist plots, indicating that T23 with the lowest charge-transfer resistance ($R_{ct}$) [57,58]. Electron paramagnetic resonance (EPR) spectra were used to validate the existence of $Ti^{III}$ under irradiation relative to the EPR signal in the dark, indicating the conversion of $Ti^{IV}$ and $Ti^{III}$ in the photocatalytic reaction [59]. As revealed in Fig. S26, T23 shows the strongest EPR signal under irradiation, indicating that T23 possesses more $Ti^{III}$ in the photoreduction system and the $Ti^{III}$ have strong reducibility to achieve the conversion of $CO_2$ to CO and $CH_4$.

{110}/{111} co-exposed facets achieves the optimal yields of CO (15.49 $\mu mol\,g^{-1}\,h^{-1}$) and $CH_4$ (5.46 $\mu mol\,g^{-1}\,h^{-1}$), which are 10 and 18 times higher than T1 with only {001} facet exposed. And the effectiveness of photo-electrons reached 74.66 $\mu mol\,g^{-1}\,h^{-1}$ for T23 (Fig. 4b). The quantum yields (QY%) over T23 are 0.26 % and 0.37 % for CO and $CH_4$, respectively (Table S4). The photocatalytic activity was comparable to the previously reported ones under the similar liquid-phase reaction without photosensitizer and also higher than that of some typical MOFs photocatalysts (Table S6). There is no liquid product
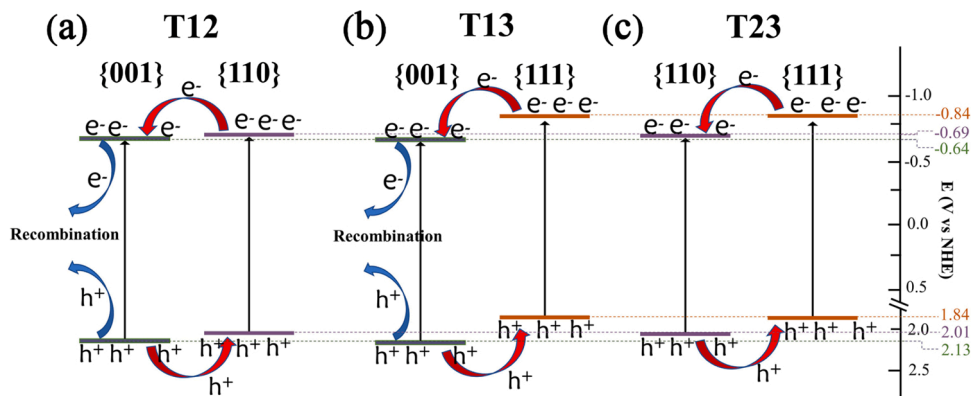


**Fig. 7.** Band structure and charge transfer of mixed facets T12 (a), T13 (b) and T23 (c).

## 3.6. DFT calculations

Gibbs free energy calculations were further carried out by building models of (001), (110) and (111) surfaces to study the possible $CO_2$-to-CO and $CO_2$-to-$CH_4$ reaction pathways for the MIL-125-$NH_2$(Ti) enclosed by low-index {001}, {110} and {111} facets. According to the results shown in Fig. 6, the formation of *COOH intermediates on (001) and (110) surfaces are endothermic steps, with the 1.52 and 1.69 eV uphill in free energy, respectively, which are the rate-limiting step for both facets. The (111) surface of MIL-125-$NH_2$(Ti) has a *COOH formation energy with 0.35 eV lower than the other two surfaces. The *COOH intermediate could be attacked by the proton-electron pair ($H^+$ + $e^-$) to form the *CO species with the first $H_2O$ desorption simultaneously. The CO molecules could be relatively easily desorbed from the MIL-125-$NH_2$(Ti) to form free CO molecules with the CO binding energy of -0.14, -0.27, and -0.23 eV on (001), (110) and (111) surfaces, respectively, which is in agreement with the experiments. Then, the proton-electron pair could attack the C or O atom of *CO to form the *CHO or COH* intermediates, respectively. In contrast, the formation energy of *COH is relatively high on three facets. This suggests that the *CHO intermediate is energetically more favorable in this process. The subsequent protonation steps, including reducing *CHO to *$CH_2O$ and *$CH_3O$ are thermodynamically favorable with the free energies downhill.

The formation of *$CH_3OH$ is an endothermic process on (001), (110) and (111) surfaces, with the free energy uphill of 0.15, 0.88 and 0.82 eV, respectively, which is the rate-limiting step for (111) surface of MIL-125-$NH_2$(Ti). The *$CH_3OH$ intermediate is reduced by the hydrogen atom to generate the *$CH_3$ along with desorption of the second $H_2O$ molecule. Finally, *$CH_3$ could react with the proton-electron pair to generate $CH_4$ to complete the catalytic pathway. Therefore, the possible reaction pathway on three low-index facets of MIL-125-$NH_2$(Ti) could be *$CO_2$ → *COOH → *CO → *CHO → *$CH_2O$ → *$CH_3O$ → *$CH_3OH$ → *$CH_3$ → *$CH_4$. The optimized geometric structures of intermediates on (001), (110) and (111) surfaces are exhibited in Figs. S27-S29, respectively. Among the three surfaces of MIL-125-$NH_2$(Ti), the (111) surface shows the lowest Gibbs free energy change of rate-limiting step, which indicated that the photocatalyst made up of (111) surfaces could be more efficient for $CO_2$ conversion, in agreement with the experimental results. Thus, the calculation results give a reasonable explanation that higher $CO_2$ reduction efficiency of {111} facets than {001} and {110} facets, meanwhile, revealed an eight-electron transfer process involving $CH_4$ evolution on the MIL-125-$NH_2$(Ti) facets.

In addition, the transfer ways of the electrons and holes after irradiation should be further discussed for the MIL-125-$NH_2$(Ti) with mixed low-index facets. T12, T13 and T23 are constructed by two facets, and their band structures are determined by using HOMO-LUMO gap derived from the UV–vis diffuse reflectance spectra (DRS) (Figs. S12 and S13) and the band edge position obtained from the Mott-Schottky plots (Fig. S14) of each composed facet. For T23, the electron was excited on the {111} facets under irradiation and quickly migrated to the {110} facets thanks to the matched band structure between {110} and {111} facets (Fig. 7c), which could effectively inhibit the recombination of electron-hole pairs, prolonging the lifetime of photogenerated electrons. Thus, it enhances photocatalytic activity [16]. T12 and T13, have {001} facets exposed on the surface and possess the decreased photocatalytic activity compared with T2 and T3, respectively. Combined with band structure (Fig. 7a and b) and PL intensity, it is indicated that the {001} facet plays the role of recombination centers for photogenerated charge carriers and thus inhibits the charge separation [60]. Thus, the formation of facet surface heterojunction is one of the factors for the photocatalytic abilities of $CO_2$ conversion.

## 4. Conclusions

In summary, MIL-125-$NH_2$(Ti), a well-used photocatalyst [61–63],

was utilized as a model for the systematic investigation on the impact of the low-index facets exposed on the photoreduction of $CO_2$. PDOS calculations were used to ensure the potential of MIL-125-$NH_2$(Ti) for photocatalytic applications. In the photocatalytic system, $Ti^{III}$ shows strong reducibility for $CO_2$-to-CO and $CO_2$-to-$CH_4$. The {111}/{110} mixture facets co-exposed exhibit excellent catalytic activity due to the formation of surface heterojunction and are in favor of the interfacial charge transfer. Thus, the regulation and optimization of facets are critical to the photocatalytic performance, which is beneficial to the initiation of the photocatalytic reaction, the promotion of electron migration and the inhibition of charge recombination. DFT calculations further revealed the energetically favorable reduction reaction pathway and proposed that {111} facets with lower energy input compared with {001} and {110} facets in the photocatalytic reaction. In short, this work uncovered the importance of morphorgy/facet on the catalytic activity as well as the facet heterojunction in boosting photocatalytic $CO_2$ reduction.

## CRediT authorship contribution statement

**Xiao-Mei Cheng:** Investigation, Validation, Data curation, Writing - original draft, Visualization. **Yuming Gu:** Formal analysis. **Xiao-Yu Zhang:** Investigation. **Xiao-Yao Dao:** Investigation, Validation. **Shi-Qing Wang:** Investigation, Validation. **Jing Ma:** Formal analysis, Writing - review & editing. **Jing Zhao:** Writing - review & editing, Supervision. **Wei-Yin Sun:** Conceptualization, Resources, Writing - review & editing, Supervision.

## Declaration of Competing Interest

The authors report no declarations of interest.

## Acknowledgments

## Appendix A. Supplementary data

Supplementary material related to this article can be found, in the online version, at doi:https://doi.org/10.1016/j.apcatb.2021.120524.

## References

[1] C. Fu, F. Li, J.C. Zhang, D. Li, K. Qian, H. Liu, J.W. Tang, F.T. Fan, Q. Zhang, X.-Q. Gong, et al., Site sensitivity of interfacial charge transfer and photocatalytic efficiency in photocatalysis: methanol oxidation on anatase $TiO_2$ nanocrystals, Angew. Chem. Int. Ed. 60 (2021) 6160–6169, https://doi.org/10.1002/anie.202014037.

[2] Y.A. Wu, I. McNulty, C. Liu, K.C. Lau, Q. Liu, A.P. Paulikas, C.-J. Sun, Z.H. Cai, J.R. Guest, Y. Ren, et al., Facet-dependent active sites of a single $Cu_2O$ particle photocatalyst for $CO_2$ reduction to methanol, Nat. Energy 4 (2019) 957–968, https://doi.org/10.1038/s41560-019-0490-3.

[3] L. Wu, Q. Wang, T.-T. Zhuang, Y. Li, G.Z. Zhang, G.-Q. Liu, F.-J. Fan, L. Shi, S.H. Yu, Single crystalline quaternary sulfide nanobelts for efficient solar-to-hydrogen conversion, Nat. Commun. 11 (2020) 5194–5201, https://doi.org/10.1038/s41467-020-18679-z.

[4] L.Z. Jiang, K.L. Liu, S.F. Hung, L.Y. Zhou, R.X. Qin, Q.H. Zhang, P.X. Liu, L. Gu, H.M. Chen, G. Fu, et al., Facet engineering accelerates spillover hydrogenation on highly diluted metal nanocatalysts, Nat. Nanotechnol. 15 (2020) 848–853, https://doi.org/10.1038/s41565-020-0746-x.

[5] A. Wang, S.J. Wu, J.L. Dong, J.W. Wang, J.L. Zhang, S.X. Zhong, S. Bai, Interfacial facet engineering on the Schottky barrier between plasmonic Au and $TiO_2$ in boosting the photocatalytic $CO_2$ reduction under ultraviolet and visible light

irradiation, Chem. Eng. J. 404 (2021) 127145–127153, https://doi.org/10.1016/j.cej.2020.127145.

[6] S.C. Wang, G. Liu, L.Z. Wang, Crystal facet engineering of photoelectrodes for photoelectrochemical water splitting, Chem. Rev. 119 (2019) 5192–5247, https://doi.org/10.1021/acs.chemrev.8b00584.

[7] D.Z. Zhong, Z.-J. Zhao, Q. Zhao, D.F. Cheng, B. Liu, G. Zhang, W.Y. Deng, H. Dong, L. Zhang, J.K. Li, et al., Coupling of Cu(100) and (110) facets promotes carbon dioxide conversion to hydrocarbons and alcohols, Angew. Chem. Int. Ed. 60 (2021) 4879–4885, https://doi.org/10.1002/anie.202015159.

[8] G.-M. Fernando, G.-F. Carlos, P.S. Juan, H. Adriam, W. Andrew, W. Iradwikanari, B. Florian, R.M. Lindsay, S. Mikhail, P. Sebastian, et al., Catalytic oxidation of CO on a curved Pt(111) surface: simultaneous ignition at all facets through a transient CO-O complex, Angew. Chem. Int. Ed. 59 (2020) 20037–20043, https://doi.org/10.1002/anie.202007195.

[9] N. Tian, Z.-Y. Zhou, S.-G. Sun, Y. Ding, Z.L. Wang, Synthesis of tetrahexahedral platinum nanocrystals with high-index facets and high electro-oxidation activity, Science 316 (2007) 732–735, https://doi.org/10.1126/science.1140484.

[10] H.G. Yang, C.H. Sun, S.Z. Qiao, J. Zou, G. Liu, S.C. Smith, H.M. Cheng, G.Q. Lu, Anatase $TiO_2$ single crystals with a large percentage of reactive facets, Nature 453 (2008) 638–641, https://doi.org/10.1038/nature06964.

[11] Y.-K. Peng, Y.C. Hu, H.-L. Chou, Y.Y. Fu, I.F. Teixeira, L. Zhang, H.Y. He, S.C. E. Tsang, Mapping surface-modified titania nanoparticles with implications for activity and facet control, Nat. Commun. 8 (2017) 675–687, https://doi.org/10.1038/s41467-017-00619-z.

[12] S.J. Liu, C. Zhang, Y.D. Sun, Q. Chen, L.F. He, K. Zhang, J. Zhang, B. Liu, L.-F. Chen, Design of metal-organic framework-based photocatalysts for hydrogen generation, Coord. Chem. Rev. 413 (2020), https://doi.org/10.1016/j.ccr.2020.213266, 213266-213242.

[13] P. Yan, J. Long, K.L. Li, S.D. Yuan, Y.J. Liu, Y.Q. Chen, The regulation of reaction processes and rate-limiting steps for efficient photocatalytic $CO_2$ reduction into methane over the tailored facets of $TiO_2$, Catal. Sci. Technol. 9 (2019) 1451–1456, https://doi.org/10.1039/C8CY02457J.

[14] X.G. Han, Q. Kuang, M.S. Jin, Z.X. Xie, L.S. Zheng, Synthesis of titania nanosheets with a high percentage of exposed (001) facets and related photocatalytic properties, J. Am. Chem. Soc. 131 (2009) 3152–3153, https://doi.org/10.1021/ja8092373.

[15] N.Q. Wu, J. Wang, D.N. Tafen, H. Wang, J.-G. Zheng, J.P. Lewis, X.G. Liu, S. S. Leonard, A. Manivannan, A. Shape-enhanced photocatalytic activity of single-crystalline anatase $TiO_2$ (101) nanobelts, J. Am. Chem. Soc. 132 (2010) 6679–6685, https://doi.org/10.1021/ja909456f.

[16] J.G. Yu, J.X. Low, W. Xiao, P. Zhou, M. Jaroniec, Enhanced photocatalytic $CO_2$-reduction activity of anatase $TiO_2$ by coexposed {001} and {101} facets, J. Am. Chem. Soc. 136 (2014) 8839–8842, https://doi.org/10.1021/ja5044787.

[17] L.-Y. Wu, Y.-F. Mu, X.-X. Guo, W. Zhang, Z.-M. Zhang, T.-B. Lu, Encapsulating perovskite quantum dots in iron-based metal-organic frameworks (MOFs) for efficient photocatalytic $CO_2$ reduction, Angew. Chem. Int. Ed. 60 (2021) 409–414, https://doi.org/10.1002/anie.202011068.

[18] X.-Y. Dao, J.-H. Guo, X.-Y. Zhang, S.-Q. Wang, X.-M. Cheng, W.-Y. Sun, Structure-dependent iron-based metal-organic frameworks for selective $CO_2$-to-$CH_4$ photocatalytic reduction, J. Mater. Chem. A Mater. Energy Sustain. 8 (2020) 25850–25856, https://doi.org/10.1039/D0TA10278D.

[19] J. Xu, S. He, H.L. Zhang, J. Huang, H.X. Lin, X.X. Wang, J.L. Long, Layered metal-organic framework/graphene nanoarchitectyres for organic photosynthesis under visible light, J. Mater. Chem. A Mater. Energy Sustain. 3 (2015) 24261, https://doi.org/10.1039/C5TA06838J.

[20] J.M. Yu, L.-H. Xie, J.-R. Li, Y.G. Ma, J.M. Seminario, P.B. Balbuena, $CO_2$ capture and separations using MOFs: computational and experimental studies, Chem. Rev. 117 (2017) 9674–9754, https://doi.org/10.1039/C9TA10575A.

[21] F. Guo, Y.-P. Wei, S.-Q. Wang, X.-Y. Zhang, F.-M. Wang, W.-Y. Sun, Pt nanoparticles embedded in flowerlike $NH_2$-UiO-68 for enhanced photocatalytic carbon dioxide reduction, J. Mater. Chem. A 7 (2019) 26490–26495, https://doi.org/10.1039/C9TA10575A.

[22] Y. Benseghir, A. Lemarchand, M. Duguet, P. Mialane, M. Gomez-Mingot, C. Roch-Marchal, T. Pino, M.-H. Ha-Thi, M. Haouas, M. Fontecave, et al., Co-immobilization of a Rh catalyst and a keggin polyoxometalate in the UiO-67 Zr-based metal-organic framework: in depth structural characterization and photocatalytic properties for $CO_2$ reduction, J. Am. Chem. Soc. 142 (2020) 9428–9438, https://doi.org/10.1021/jacs.0c02425.

[23] X. Ma, L. Wang, Q. Zhang, H.-L. Jiang, Switching on the photocatalysis of metal-organic frameworks by engineering structural defects, Angew. Chem. Int. Ed. 58 (2019) 12175–12179, https://doi.org/10.1002/anie.201907074.

[24] L. Liu, Z. Chen, J. Wang, D. Zhang, Y. Zhu, S. Ling, K.W. Huang, Y. Belmabkhout, K. Adil, Y. Zhang, et al., Imaging defects and their evolution in a metal-organic framework at sub-unit-cell resolution, Nat. Chem. 11 (2019) 622–628, https://doi.org/10.1038/s41557-019-0263-4.

[25] Y.-Z. Chen, Z.U. Wang, H. Wang, J. Lu, S.-H. Yu, H.-L. Jiang, Singlet oxygen-engaged selective photo-oxidation over Pt nanocrystals/porphyrinic MOF: the roles of photothermal effect and Pt electronic state, J. Am. Chem. Soc. 139 (2017) 2035–2044, https://doi.org/10.1021/jacs.6b12074.

[26] I.I. Alkhatib, C. Garlisi, M. Pagliaro, K. Al-Ali, G. Palmisano, Metal-organic frameworks for photocatalytic $CO_2$ reduction under visible radiation: a review of strategies and applications, Catal. Today 340 (2020) 209–224, https://doi.org/10.1016/j.cattod.2018.09.032.

[27] C.A. Trickett, A. Helal, B.A. Al-Maythalony, Z.H. Yamani, K.E. Cordova, O. M. Yaghi, The chemistry of metal-organic frameworks for CO2 capture,

[28] L.Z. Liu, S.B. Wang, H.W. Huang, Y.H. Zhang, T.Y. Ma, Surface sites engineering on semiconductors to boost photocatalytic $CO_2$ reduction, Nano Energy 75 (2020) 104959–104980, https://doi.org/10.1016/j.nanoen.2020.104959.

[29] H.W. Zhang, L. Ma, J.T. Ming, B.Q. Liu, Y.B. Zhao, Y.D. Hou, Z.X. Ding, C. Xu, Z. Z. Zhang, J.L. Long, Amorphous $Ta_2O_xN_y$-enwrapped $TiO_2$ rutile nanorods for enhanced solar photoelectrochemical water splitting, Appl. Catal. B 243 (2019) 481–489, https://doi.org/10.1016/j.apcatb.2018.10.024.

[30] X.-M. Cheng, X.-Y. Dao, S.-Q. Wang, J. Zhao, W.-Y. Sun, Enhanced photocatalytic $CO_2$ reduction activity over $NH_2$-MIL-125(Ti) by facet regulation, ACS Catal. 11 (2020) 650–658, https://doi.org/10.1021/acscatal.0c04426.

[31] G. Kresse, J. Furthmuller, Efficiency of ab-initio total energy calculations for metal and semiconductors using a plane-wave basis set, Comput. Mater. Sci. 6 (1996) 15–50, https://doi.org/10.1016/0927-0256(96)00008-0.

[32] G. Kresse, J. Furthmuller, Efficient iterative schemes for ab initio total-energy calculations using a plane-wave basis set, Phys. Rev. B 54 (1996) 11169–11186, https://doi.org/10.1103/PhysRevB.54.11169.

[33] J.P. Perdew, K. Burke, M. Ernzerhof, Generation gradient approximation made simple, Phys. Rev. Lett. 77 (1996) 3865–3868, https://doi.org/10.1103/PhysRevLett.77.3865.

[34] S. Grimme, J. Antony, S. Ehrlich, H. Krieg, A consistent and accurate ab initio parametrization of density functional dispersion correction (DFT-D) for the 94 element H-Pu, J. Chem. Phys. 132 (2010) 154104–154119, https://doi.org/10.1063/1.3382344.

[35] S. Grimme, S. Ehrlich, L. Goerigk, Effect of the damping function in dispersion corrected density functional theory, J. Comput. Chem. 32 (2011) 1456–1465, https://doi.org/10.1002/jcc.21759.

[36] S. Dudarev, G. Botton, S. Savrasov, C. Humphreys, A. Sutton, Electron-energy-loss spectra and the structural stability of nickel oxide: an LSDA + U study, Phys. Rev. B 57 (1998), https://doi.org/10.1103/PhysRevB.57.1505, 1505.

[37] J. Chang, Z.-Y. Jiang, Z.-Y. Zhang, Y.-M. Lin, P.-L. Tian, B. Zhou, L. Chen, Theoretical studies of photocatalytic behaviors of isoelectronic C/Si/Ge/Sn-doped $TiO_2$: DFT + U, Appl. Surf. Sci. 484 (2019) 1304–1309, https://doi.org/10.1016/j.apsusc.2018.12.252.

[38] K.Z. Qi, X.H. Xing, A. Zada, M.Y. Li, Q. Wang, S.-Y. Liu, H.X. Lin, G.Z. Wang, Transition metal doped ZnO nanoparticles with enhanced photocatalytic and antibacterial performances: experimental and DFT studies, Cerm. Int. 46 (2020) 1494–1520, https://doi.org/10.1016/j.ceramint.2019.09.116.

[39] W.L. Yu, J.F. Zhang, T.Y. Peng, New insight into the enhanced photocatalytic activity of N-, C- and S-doped ZnO photocatalysts, Appl. Catal. B 181 (2016) 220–227, https://doi.org/10.1016/j.apcatb.2015.07.031.

[40] D.Y. Shi, R. Zheng, M.-J. Sun, X.R. Cao, C.-X. Sun, C.-J. Cui, C.-S. Liu, J.W. Zhao, M. Du, Semiconductive copper(I)–Organic frameworks for efficient light-driven hydrogen generation without additional photosensitizers and cocatalysts, Angew. Chem. Int. Ed. 56 (2017) 14637–14646, https://doi.org/10.1002/anie.201709869.

[41] M.-H. Du, Density functional calculations of native defects in $CH_3NH_3PbI_3$: effects of spin-orbit coupling and self-interaction error, J. Phys. Chem. Lett. 6 (2015) 1461–1466, https://doi.org/10.1021/acs.jpclett.5b00199.

[42] P.N. Paulino, V.M.M. Salim, N.S. Resende, Zn-Cu promoted $TiO_2$ photocatalyst for $CO_2$ reduction with $H_2O$ under UV light, Appl. Catal. B 185 (2016) 362–370, https://doi.org/10.1016/j.apcatb.2015.12.037.

[43] L. Zhang, L.J. Zhang, Y.M. Chen, Y.K. Zheng, J. Guo, S.L. Wan, S. Wang, C.K. Ngaw, J.D. Lin, Y. Wang, CdS/ZnO: a multipronged approach for efficient reduction of carbon dioxide under visible light irradiation, ACS Sustainable Chem. Eng. 8 (2020) 5270–5277, https://doi.org/10.1021/acssuschemeng.0c00190.

[44] Y.J. Gao, L. Zhang, Y.M. Gu, W.W. Zhang, Y. Pan, W.H. Fang, J. Ma, Y.-Q. Lan, J. F. Bai, Formation of a mixed-valence Cu(I)/Cu(II) metal-organic framework with the full light spectrum and high selectivity of $CO_2$ photoreduction into $CH_4$, Chem. Sci. 11 (2020) 10143–10148, https://doi.org/10.1039/D0SC03754K.

[45] Y.H. Fu, D.R. Sun, Y.J. Chen, R.K. Huang, Z.X. Ding, X.Z. Fu, Z.H. Li, An amine-functionalized titanium metal-organic framework photocatalyst with visible-light-Induced activity for $CO_2$ reduction, Angew. Chem., Int. Ed. 51 (2012) 3364–3367, https://doi.org/10.1002/anie.201108357.

[46] Neil W. Ashcroft, N.D. Mermin, Solid State Physics New York: Holt, Rinehart and Winston ISBN 0030839939.

[47] J. Park, M. Shirai, G.Y. Jung, S.O. Park, M. Park, J. Ryu, S.K. Kwak, J. Cho, Correlation of low-index facets to active sites in micrometer-sized polyhedral pyrochlore electrocatalyst, ACS Catal. 8 (2018) 9647–9655, https://doi.org/10.1021/acscatal.8b01725.

[48] Z.M. Yang, S.D. Sun, C.C. Kong, X.P. Song, B.J. Ding, Designated-tailoring on {100} facets of $Cu_2O$ nanostructures: from octahedral to its different truncated forms, J. Nanomater. 2010 (2010) 1–11, https://doi.org/10.1155/2010/710584.

[49] H.G. Yang, H.C. Zeng, Self-construction of hollow $SnO_2$ octahedra based on two-dimensional aggregation of nanocrystallites, Angew. Chem. Int. Ed. 43 (2004) 5930–5933, https://doi.org/10.1002/ange.200461129.

[50] S. Karmakar, S. Barman, F.A. Rahimi, T.K. Maji, Covalent grafting of molecular photosensitizer and catalyst on MOF-808: effect of pore confinement toward visible light-driven $CO_2$ reduction in water, Energy Environ. Sci. 14 (2021) 2429–2440, https://doi.org/10.1039/D0EE03643A.

[51] J. Wang, A.S. Cherevan, C. Hannecart, S. Naghdi, S.P. Nandan, T. Gupta, D. Eder, Ti-based MOFs: new insight on the impact of ligand composition and hole scavengers on stability, charge separation and photocatalytic hydrogen evolution, Appl. Catal. B 283 (2021), https://doi.org/10.1016/j.apcatb.2020.119626, 119626.

[52] H.-Q. Xu, J.H. Hu, D.K. Wang, Z.H. Li, Q. Zhang, Y. Luo, S.-H. Yu, H.-L. Jiang, Visible-light photoreduction of $CO_2$ in a metal-organic framework: boosting electron-hole separation via Electron trap states, J. Am. Chem. Soc. 137 (2015) 13440–13443, https://doi.org/10.1021/jacs.5b08773.

[53] Z.Y. Wu, X.B. Huang, H.Y. Zheng, P. Wang, G.T. Hai, W.J. Dong, G. Wang, Aromatic heterocycle-grafted $NH_2$-MIL-125(Ti) via conjugated linker with enhanced photocatalytic activity for selective oxidation of alcohols under visible light, Appl. Catal. B 224 (2018) 479–487, https://doi.org/10.1016/j.apcatb.2017.10.034.

[54] Q.J. Xiang, B. Cheng, J.G. Yu, Graphene-based photocatalysts for solar-fuel generation, Angew. Chem. Int. Ed. 54 (2015) 11350–11366, https://doi.org/10.1002/anie.201411096.

[55] J.W. Zhao, B.Q. Liu, L.S. Meng, S. He, R.S. Yuan, Y.D. Hou, Z.X. Ding, Z.Z. Zhang, X.X. Wang, J.L. Long, Plasmonic control of solar-driven $CO_2$ conversion at the metal/ZnO interfaces, Appl. Catal. B 256 (2019) 117823, https://doi.org/10.1016/j.apcatb.2019.117823.

[56] X. Chen, Q. Dang, R.J. Sa, L.Y. Li, J.H. Bi, Z.Z. Zhang, J.L. Long, Y. Yu, Z.G. Zou, Integrating single Ni sites into biomimetic networks of covalent organic frameworks for selective photoreduction of $CO_2$, Chem. Sci. 11 (2020) 6915, https://doi.org/10.1039/D0SC01747G.

[57] H.W. Zhang, J.T. Ming, J.W. Zhao, Q. Gu, C. Xu, Z.X. Ding, R.S. Yuan, Z.Z. Zhang, H.X. Lin, X.X. Wang, J.L. Long, High-rate, tunable syngas production, with artificial photosynthetic cell, Angew. Chem. Int. Ed. 58 (2019) 7718–7722, https://doi.org/10.1002/anie.201902361.

[58] Y.-N. Gong, W.H. Zhong, Y. Li, Y.Z. Qiu, L.R. Zheng, J. Jiang, H.L. Jiang, Regulating photocatalysis by spin-state manipulation of cobalt in covalent organic

[59] M.A. Nasalevich, R. Becker, E.V. Ramos-Fernandez, S. Castellanos, S.L. Veber, M. V. Fedin, F. Kapteijn, J.N.H. Reek, J.I. van der Vlugt, J. Gascon, Co@$NH_2$-MIL-125 (Ti): cobaloxime-derived metal-organic framework-based composite for light-driven $H_2$ production, Energy Environ. Sci. 8 (2015) 364–375, https://doi.org/10.1039/C4EE02853H.

[60] S.C. Sun, P. Gao, Y.R. Yang, P.P. Yang, Y.J. Chen, Y.B. Wang, N-doped $TiO_2$ nanobelts with coexposed (001) and (101) facets and their highly efficient visible-light-driven photocatalytic hydrogen production, ACS Appl. Mater. Interfaces 8 (2016) 18126–18131, https://doi.org/10.1021/acsami.6b05244.

[61] D.R. Sun, W.J. Liu, Y.H. Fu, Z.X. Fang, F.X. Sun, X.Z. Fu, Y.F. Zhang, Z.H. Li, Noble metals can have different effects on photocatalysis over metal-organic frameworks (MOFs): a case study on M/$NH_2$-MIL-125(Ti) (M=Pt and Au), Chem. Eur. J. 20 (2014) 4780–4788, https://doi.org/10.1002/chem.201304067.

[62] M.B. Chambers, X. Wang, L. Ellezam, O. Ersen, M. Fontecave, C. Sanchez, L. Rozes, C. Mellot-Draznieks, Maximizing the photocatalytic activity of metal-organic frameworks with aminated-functionalized linkers: substoichiometric effects in MIL-125-$NH_2$, J. Am. Chem. Soc. 139 (2017) 8222–8228, https://doi.org/10.1021/jacs.7b02186.

[63] B.X. Zhang, J.L. Zahng, X.N. Tan, D. Shao, J.B. Shi, L.R. Zheng, J. Zhang, G.Y. Yang, B.X. Han, MIL-125-$NH_2$@$TiO_2$ core-shell particles produced by a post-solvothermal route for high-performance photocatalytic $H_2$ production, ACS Appl. Mater. Interfaces 10 (2018) 16418–16423, https://doi.org/10.1021/acsami.8b01462.